

Ultrasonic backscatter coefficient quantitative estimates from high-concentration Chinese hamster ovary cell pellet biophantoms

Aiguo Han, Rami Abuhabsh, James P. Blue, Jr., Sandhya Sarwate, and William D. O'Brien, Jr.^{a)}

Bioacoustics Research Laboratory, Department of Electrical and Computer Engineering, University of Illinois at Urbana-Champaign, 405 North Mathews, Urbana, Illinois 61801

(Received 13 May 2011; revised 29 September 2011; accepted 3 October 2011)

Previous work estimated the ultrasonic backscatter coefficient (BSC) from low-concentration (volume density < 3%) Chinese Hamster Ovary (CHO, 6.7- μm cell radius) cell pellets. This study extends the work to higher cell concentrations (volume densities: 9.6% to 63%). At low concentration, BSC magnitude is proportional to the cell concentration and BSC frequency dependency is independent of cell concentration. At high cell concentration, BSC magnitude is not proportional to cell concentration and BSC frequency dependency is dependent on cell concentration. This transition occurs when the volume density reaches between 10% and 30%. Under high cell concentration conditions, the BSC magnitude increases slower than proportionally with the number density at low frequencies ($ka < 1$), as observed by others. However, what is new is that the BSC magnitude can increase either slower or faster than proportionally with number density at high frequencies ($ka > 1$). The concentric sphere model least squares estimates show a decrease in estimated cell radius with number density, suggesting that the concentric spheres model is becoming less applicable as concentration increases because the estimated cell radius becomes smaller than that measured. The critical volume density, starting from when the model becomes less applicable, is estimated to be between 10% and 30% cell volume density. © 2011 Acoustical Society of America. [DOI: 10.1121/1.3655879]

PACS number(s): 43.80.Cs, 43.80.Qf, 43.80.Vj [CCC]

Pages: 4139–4147

I. INTRODUCTION

Quantitative ultrasound (QUS) utilizes the frequency-dependent information to yield quantitative tissue properties such as scatterer size, shape, number density, and acoustic impedance. As a model-based imaging approach, QUS requires the identification of scattering sites and appropriate models to accurately describe ultrasonic scattering in biological materials.

There have been efforts to understand scattering sites and determine the appropriate scattering models. It has been hypothesized that the cell is the dominating scattering site (Oelze and Zachary, 2006); likewise, the nucleus has been hypothesized (Kolios *et al.*, 2004; Czarnota and Kolios, 2010). Both hypotheses can be modeled with a fluid-filled sphere model where the cell (or the nucleus) is modeled as a homogeneous fluid sphere embedded in the fluid background having acoustic properties that are different from those of the sphere.

There have also been efforts to understand scattering using approaches such as three-dimensional acoustic impedance map (3DZM) (Mamou *et al.*, 2005; Dapore *et al.*, 2011; Pawlicki *et al.*, 2011), single cell scattering (Baddour *et al.*, 2005; Falou *et al.*, 2010), dilute cell solution (Tunis *et al.*, 2005), isolated nuclei (Taggart *et al.*, 2007), dense cell

aggregate (Taggart *et al.*, 2007), and numerical simulations (Doyle *et al.*, 2009). Inspired by the physical phantoms, biophantoms likewise have been used as a technique to elucidate scattering phenomena. Physical phantoms have been used to study the applicability of acoustic scattering theories wherein BSC estimates have shown good agreement with theoretical predictions (Anderson *et al.*, 2010; King *et al.*, 2010). Therefore, biophantoms, which are more random (less controlled) than physical phantoms but less random (better controlled) than real tissues, have been fabricated to be used as a tool to test the applicability of scattering theories in biological materials.

Previous work (Teisseire *et al.*, 2010) has been conducted on estimating the BSC from biophantoms containing live Chinese Hamster Ovary (CHO) cells using weakly focused single-element transducers. CHO cells were chosen for biophantoms because of the similar geometry to the concentric sphere structure as well as its convenient laboratory capabilities. BSC estimates from CHO cell pellet biophantoms of relatively low cell concentrations (1.25, 4.97, 19.5 million cells/mL [Mcell/mL]) showed good agreement with the two concentric fluid spheres theory (McNew *et al.*, 2009). A least squares analysis was performed to estimate the cell properties (size of cell and nucleus, speed of sound in cytoplasm and nucleus, density of cytoplasm and nucleus) from the BSC data. The estimated cell properties agreed well with the literature or direct measurements.

^{a)}Author to whom correspondence should be addressed. Electronic mail: wdo@illinois.edu

The previous work was based on the assumption that the cells are independent scatter sites, a reasonable assumption if the cell concentration is low. As the cell concentration increases, this assumption may become less valid. The cells may interact with each other acoustically when they are close to each other. Multiple scattering could be nonnegligible (Aubry *et al.*, 2008; Doyle *et al.*, 2009; Aubry and Derode, 2011). The geometry, structure or acoustic properties of the cell and its components may have changed. Coherent scattering may also play a role because the positions of cells may not be random any more due to close distances between cells (Hunt *et al.*, 2002). Although the acoustic scattering under the high-concentration condition is complicated, it is meaningful and necessary to study because it more closely matches real tissue. Therefore, this paper extends the cell pellet study from low cell concentrations to high cell concentrations.

This paper summarizes the study of 18 CHO cell pellets of six different number densities (1.25, 4.97, 19.5, 72.3, 224, 473 Mcell/mL), with three separate cell pellet samples per number density. The BSC estimates of those cell pellets are made, and the concentric sphere model is applied. In addition to the high-concentration condition, this work improves the previous work also in the following ways. First, the relationship between BSC magnitude and number density is studied and compared to the BSC theory. Second, a Gaussian size distribution model is proposed from measured CHO cell and nuclear radii data, and is used for theoretical BSC determinations. The Gaussian distribution, compared to the uniform distribution used previously, is closer to the real condition. Third, the experimental setup has been improved such that more accurate data can be acquired.

II. THEORY AND SIMULATION

A. BSC theory: Identical scatterers

The BSC theory of the concentric sphere model has been discussed previously (Teisseire *et al.*, 2010) and is briefly reviewed in this section. Suppose a plane wave of amplitude P_0 is incident on a scattering volume. BSC is defined as the differential scattering cross section per unit volume of scatters at 180° and may be expressed as

$$\text{BSC}(f) = \frac{r^2}{V} \frac{|p_{\text{scat},\text{total}}(\theta = \pi)|^2}{P_0^2}, \quad (1)$$

where r is the distance from the scatterers to the observation point, which is assumed to be very large compared to the dimensions of the scattering volume, V is the scattering volume, and $|p_{\text{scat},\text{total}}(\theta = \pi)|$ is the amplitude of the total backscattered wave.

Assuming the coherent field is not taken into account (waves do not interfere), and multiple scattering is ignored, the total intensity is the sum of the individual intensities from a randomly positioned ensemble of n scatterers, which gives

$$\text{BSC}(f) = \frac{n r^2 |p_{\text{scat},i}(\theta = \pi)|^2}{V P_0^2}, \quad (2)$$

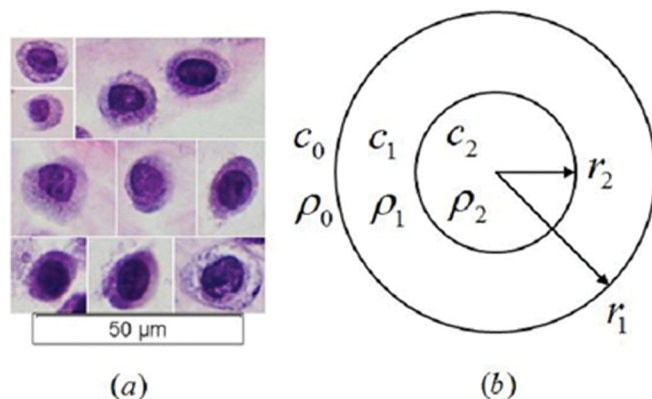


FIG. 1. (Color online) Geometries of CHO cells and the concentric sphere model (adapted from Teisseire *et al.*, 2010): (a) optical microscope images (40 x) of H&E stained CHO cells, (b) physical properties of two concentric spheres. For each cell in Fig. 1(a), the darker area at the center is the cell nucleus. The lighter ring surrounding the nucleus is the cytoplasm. In Fig. 1(b), the infinite (background) medium has density ρ_0 and sound speed c_0 . The outer sphere has density ρ_1 , sound speed c_1 and radius r_1 . The inner sphere has density ρ_2 , sound speed c_2 and radius r_2 . The three media (inner sphere, outer sphere and background) are modeled as spatially homogeneous fluids.

where the factor n/V can be expressed as \bar{n} corresponding to the number density of the ensemble, and $|p_{\text{scat},i}(\theta = \pi)|$ is the amplitude of backscattered wave of an individual scatterer.

Now consider the two concentric fluid spheres entity as a single scatterer (Fig. 1). If a plane wave of amplitude P_0 is incident on such a scatterer, then the expression of the scattered acoustic pressure $p_{\text{scat},i}$ was given by McNew *et al.* (2009). Therefore, the BSC for this concentric sphere model can be calculated by inserting $p_{\text{scat},i}$ into Eq. (2). When applied to eukaryotic cells, the outer sphere represents the cytoplasm, and the inner sphere models the nucleus.

B. BSC simulation: Size distribution

The BSC can be affected by the distribution of scatterer size (Vlad *et al.*, 2010; Saha *et al.*, 2010). In the previous paper (Teisseire *et al.*, 2010), it was assumed that the size of the CHO cells is identical and the nuclear radius follows a uniform distribution for simplicity. However, a measurement of 500 CHO cells (see Teisseire *et al.*, 2010; Sec. III A for measurement details) showed that the radii of both the cells and nuclei are better described by Gaussian distributions (Fig. 2). The cell radius is assumed to be a linear function of nuclear radius (Fig. 3) for modeling purposes.

For an ensemble of two concentric spheres, if the inner sphere radius has a Gaussian distribution with known mean and standard deviation, and if the outer sphere radius can be expressed as $r_1 = C_1 r_2 + C_2$, then the theoretical BSC can be computed by

$$\text{BSC}_{\text{dist}}(f) = \int_0^\infty g(r_2) \text{BSC}(f, C_1 r_2 + C_2, r_2) dr_2, \quad (3)$$

where $g(r_2)$ is the probability density function of the inner sphere radius.

For a Gaussian size distribution, the effect of size variance on BSC is simulated using Eq. (3) for the two

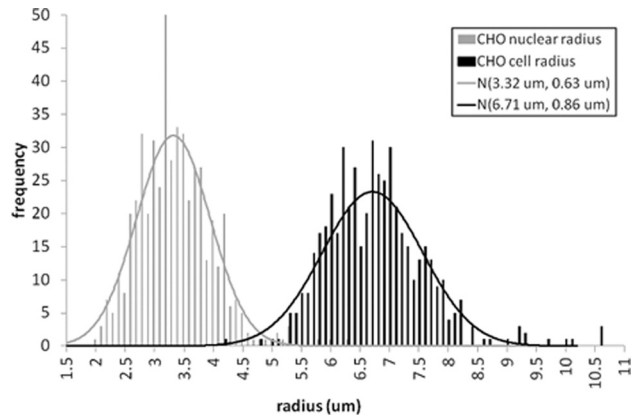


FIG. 2. Distributions of CHO cell radius and nucleus radius. The histogram results from measurements of 500 CHO cells. The measurements yielded the cell radius to have a mean of $6.71 \mu\text{m}$ and a standard deviation of $0.86 \mu\text{m}$, along with a nuclear radius mean of $3.32 \mu\text{m}$ and a standard deviation of $0.63 \mu\text{m}$. The dark and light Gaussian distribution curves are plotted to approximate the distribution of cell and nucleus radii, respectively.

concentric spheres model and shown in Fig. 4(a). In the simulation, the actual range of the inner sphere radius is limited to $[r_2 - 3\sigma, r_2 + 3\sigma]$, where r_2 and σ are the mean and standard deviation of inner sphere radius. The result shows that the size variance mainly controls the magnitude of the BSC dip at the frequency of around $kr_2 = 1$. The smallest radius variance yields the deepest BSC dip in the high-frequency range, whereas the largest radius variance yields the shallowest BSC dip. In addition, the fraction of scatters with $kr_2 > 1$ versus frequency for the four cases is shown [Fig. 4(b)] to illustrate the meaning of the std/mean ratio in the context of kr_2 .

III. METHODS

A. Experimental setup

The procedure of constructing the cell pellet biophantoms has been previously described (Teisseire *et al.*, 2010; Sec. III A). The biophantoms were ultrasonically scanned using two single-element transducers (NIH High-frequency Transducer Resource Center, University of Southern California, Los Angeles, CA, USA; see Table I).

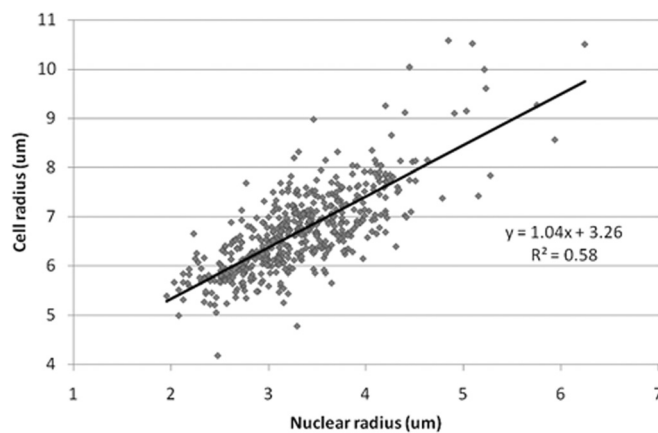
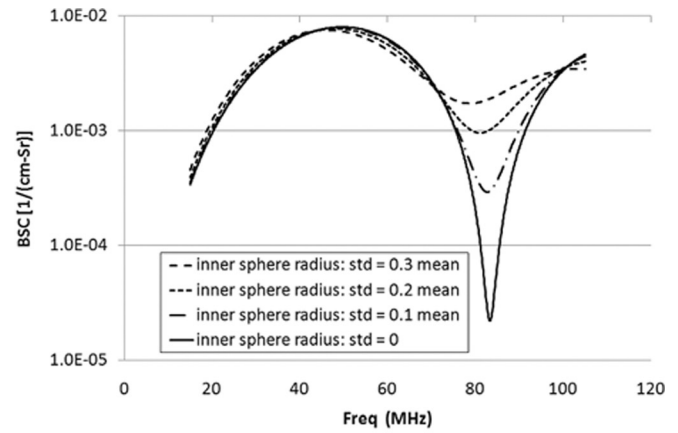
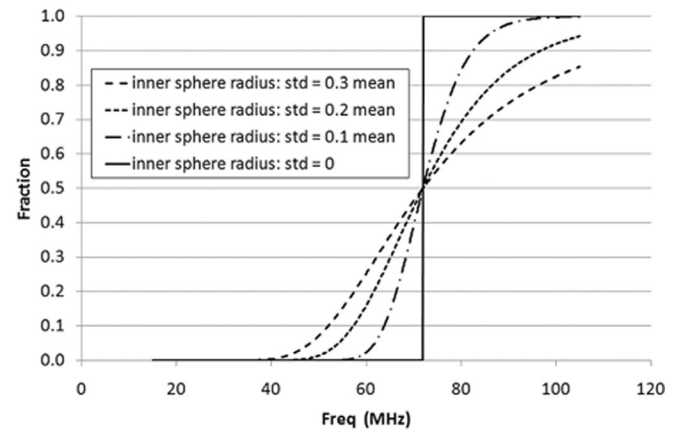


FIG. 3. Scatter diagram of cell radius and nuclear radius. The trendline shows the linear relationship between the two radii.



(a)



(b)

FIG. 4. (a) Comparison of theoretical BSC vs. frequency of different size variance for the concentric spheres model. For all the curves, the inner sphere radius r_2 has a Gaussian distribution of mean $3.32 \mu\text{m}$. The standard deviation of r_2 is set to be 0, 0.332, 0.664, and $0.996 \mu\text{m}$, respectively, for each curve, that is, 0, 0.1, 0.2, and 0.3 times the mean. The outer sphere radius r_1 is also assumed to have a Gaussian distribution, and is related to the inner sphere radius by $r_1 = 1.04r_2 + 3.26$. Thus the mean of r_1 is $6.71 \mu\text{m}$. As for the other parameters, $\bar{n} = 2 \times 10^7$ scatterers/mL, $Z_1 = 1.58 \text{ Mrayl}$ ($\rho_1 = 1.03 \text{ g/mL}$, $c_1 = 1540 \text{ m/s}$), $Z_2 = 1.61 \text{ Mrayl}$ ($\rho_2 = 1.1 \text{ g/mL}$, $c_2 = 1460 \text{ m/s}$) and $Z_0 = 1.5 \text{ Mrayl}$ ($\rho_0 = 1 \text{ g/mL}$ and $c_0 = 1500 \text{ m/s}$). (b) The fraction of scatterers with $kr_2 > 1$ versus frequency.

The transducers were driven using a UTEX UT340 pulser/receiver (UTEX Scientific Instruments Inc., Mississauga, Ontario, Canada) which operated in the pitch-catch mode. A 50DR-001 BNC attenuator (JFW Industries Inc., Indianapolis, IN, USA) was connected to the pulser to attenuate the driving pulse in order to avoid transducer saturation. A RDX-6 diplexer (Ritec Inc., Warwick, RI, USA) was used to separate the transmitted and received signals because only the transmitted signal needs to be attenuated. The transducers were moved using a precision motion control system (Daedal Parker Hannifin Corporation, Irwin, PA, USA) that has a linear spatial accuracy of $1 \mu\text{m}$. The analog echo signal was acquired using a 10-bit Agilent U1065A-002 A/D card (Agilent Technologies, Santa Clara, CA, USA) set to sample at 1 GHz.

The cell pellet is placed in a small plastic tube and wrapped with a $10\text{-}\mu\text{m}$ -thick plastic film (Saran Wrap;

TABLE I. Transducer information and characteristics.

Center frequency (MHz)	-10 dB bandwidth (MHz)	Wavelength at center frequency (μm)	f -number	-6 dB Depth of field (mm)	-6 dB Beam width (μm)	Acquisition step size (μm)
40	26–65	37.5	3.0	2.4	112.5	60
80	49–105	18.8	3.0	1.2	56.4	30

Reynolds, Richmond, VA, USA) (Fig. 5). The tube is filled with an F-12K medium (ATCC, Manassas, VA, USA) along with 8.98% of fetal bovine serum (Hyclone Laboratories, Logan, Utah, USA). Scans were performed in a tank filled with degassed water having a temperature between 21.5 and 22.5 °C. To scan the CHO biophantoms, the transducer focus was positioned in the cell pellet.

B. Data processing

The BSCs were computed from the RF echo data using the method described in [Chen *et al.* \(1997\)](#). This method is designed to remove equipment dependent effects by dividing the power spectrum of the measured data by a reference spectrum from the flat Plexiglas surface.

The best fit to the concentric sphere model was performed by minimizing the sum of the squares of the difference between theoretical and experimental BSCs. A least squares analysis was used to determine the parameters that best agreed with the experimental response in the spectral domain. Gaussian distributions are applied to both the cell and nuclear radii. The mean and standard deviation of the nuclear radius are assumed to be linked by $\text{std}/\text{mean} = 0.19$, as suggested by the real measurements (Fig. 2). The cell radius is linked to the nuclear radius by $r_1 = C_1 r_2 + C_2$, where C_1 and C_2 are parameters to be fitted. Therefore, the parameters are μ_2 (nuclear radius mean), C_1 , C_2 , ρ_1 , ρ_2 , c_1 , c_2 , and \bar{n} . The background medium was assumed to have an impedance $Z_0 = 1.5 \text{ Mrayl}$ ($\rho_0 = 1 \text{ g/mL}$ and $c_0 = 1500 \text{ m/s}$). Even though the number density \bar{n} is a quantified parameter, it is still treated as an unknown parameter in the minimization procedure, functioning as a gain factor.

The problem of fitting multiple parameters was solved by the MATLAB (The Mathworks Inc., Natick, MA, USA) nonlinear curve-fitting function “lsqcurvefit,” wherein the

trust-region-reflective algorithm was used as the nonlinear data-fitting approach.

IV. RESULTS

A. Cell concentrations

Eighteen cell pellets of six different cell concentrations were evaluated (three cell pellets per concentration). The cell concentration is represented by number density and volume density, as shown in Table II.

The number density is defined as the number of cells per unit volume of total mixed materials, i.e.,

$$\bar{n} = \frac{N}{V_{\text{cells}} + V_{\text{plasma}} + V_{\text{thrombin}}}, \quad (4)$$

where N is the total number of cells, V_{plasma} and V_{thrombin} are the volumes of plasma and of thrombin, respectively, and V_{cells} is the estimated volume of total cells. Because there is a distribution in cell radius, the volume of one cell is calculated using a sphere radius of $6.82 \mu\text{m}$, which is determined by the expression $\sqrt[3]{\text{mean}(r_1^3)}$, where r_1 is the measured cell radius.

The volume density (or volume fraction) is defined as the ratio of cell volume to pellet volume, where the volume of cells and the volume of the cell pellet are determined using the method described for the number density. Volume density reveals straightforwardly how close the number density is to the limit. Note that the higher concentrations are close to the upper limit of unity.

The cell concentration is also shown by the histology photos in Fig. 6. The figure shows that 1.25 and 4.97 Mcell/mL are relatively low cell concentrations, whereas the concentration of 473 Mcell/mL cell pellet is indeed quite close to the limiting case.

B. Cell pellet attenuation

Attenuation compensation is essential for this study because the attenuation is large at high frequencies and the

TABLE II. Summary of cell concentrations of the cell pellets.

	Number density (Mcell/mL)	Volume density (mL/mL)
Concentration 1	1.25	0.0017
Concentration 2	4.97	0.0066
Concentration 3	19.5	0.026
Concentration 4	72.3	0.096
Concentration 5	224	0.30
Concentration 6	473	0.63

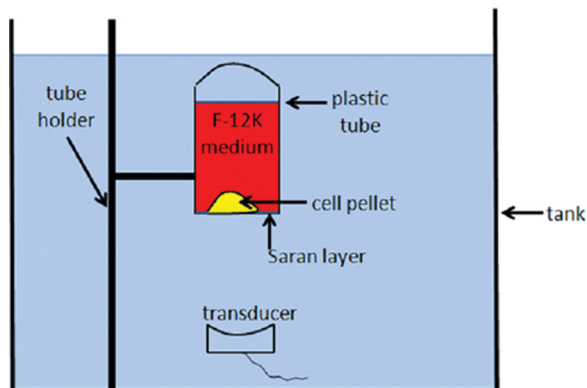


FIG. 5. (Color online) The diagram of the experimental set-up.

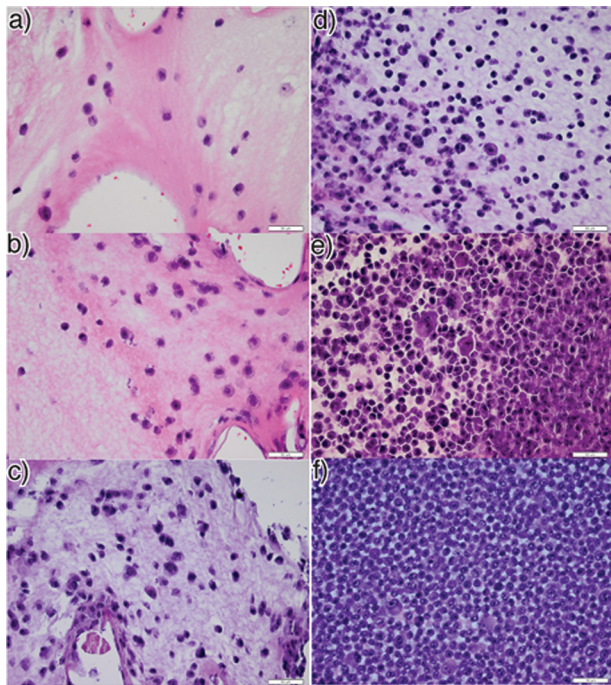


FIG. 6. (Color online) Optical microscope images (40X) of H&E stained CHO cells from: cell pellets of number density 1.25, 4.97, 19.5, 72.3, 224, 473 Mcell/mL, respectively, (a–f) Scale bars represent 50 μ m.

fit parameters can be very sensitive to the magnitude and shape of the BSC vs. frequency curves. The attenuation of the cell pellets is measured using an insertion-loss broadband technique (Wear *et al.*, 2005) for each of the two transducers (Table I). The effect of water attenuation is not negligible in the 20–100 MHz frequency range. Therefore, the following equation is used to calculate cell pellet attenuation:

$$\alpha(f) = \alpha_w(f) + \frac{20}{2d_z} \log_{10} \left(\frac{S_r(f)}{S_p(f)} \right), \quad (5)$$

where $\alpha(f)$ is the frequency-dependent attenuation (dB/cm) of the cell pellet, and $\alpha_w(f)$ is the attenuation of the F-12K medium, taken to be similar to water, $2.1715 \times 10^{-3} \text{ dB} \cdot \text{cm}^{-1} \cdot \text{MHz}^{-2}$ at 20 °C (Duck, 1990), because

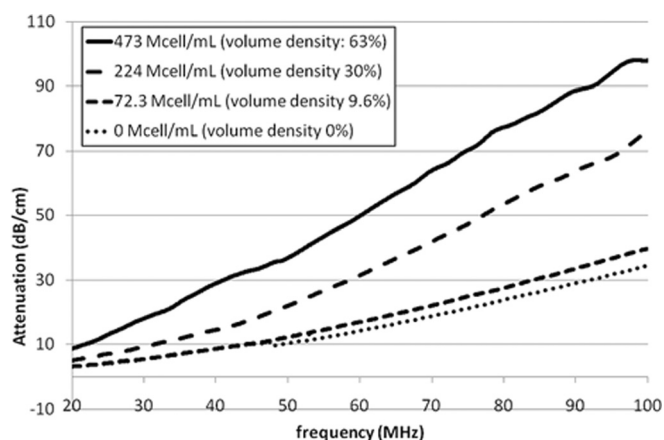


FIG. 7. CHO cell pellet attenuation vs. frequency.

TABLE III. Summary of cell pellets attenuation coefficient for various cell concentrations.

Number density	β	n
0 Mcell/mL	0.021	1.6
72.3 Mcell/mL	0.019	1.7
224 Mcell/mL	0.025	1.7
473 Mcell/mL	0.15	1.4

in-house measurements of the F-12K medium were consistent with water. d_z is the thickness of the cell pellet, and f is the frequency (MHz). $S_r(f)$ is the amplitude spectrum of the reference signal, the signal reflected back from a flat steel surface without the presence of the cell pellet. $S_p(f)$ is the amplitude spectrum of the reflected signal from the steel surface when the cell pellet is placed between the transducer and the steel surface. The cell pellet attenuation vs. frequency curves at various cell concentrations are shown in Fig. 7.

The following equation is fitted to the cell pellet attenuation vs. frequency curves:

$$\alpha(f) = \beta f^n, \quad (6)$$

where $\alpha(f)$ is in dB/cm, and f is in MHz. The fit parameters β and n for various concentrations are listed in Table III.

C. Transmission compensation

The ultrasonic transmission properties of the Saran layer were measured and employed in the transmission compensation of BSC calculation. The transmission coefficient vs. frequency curve (Fig. 8) of the three layer media (water-Saran-water) was measured using an insertion-loss broadband technique (Wear *et al.*, 2005) from 1 to 100 MHz. A reference signal was obtained using the specular reflection from Plexiglas placed at the transducer focus in degassed water. Then, a layer of Saran was inserted to the ultrasonic

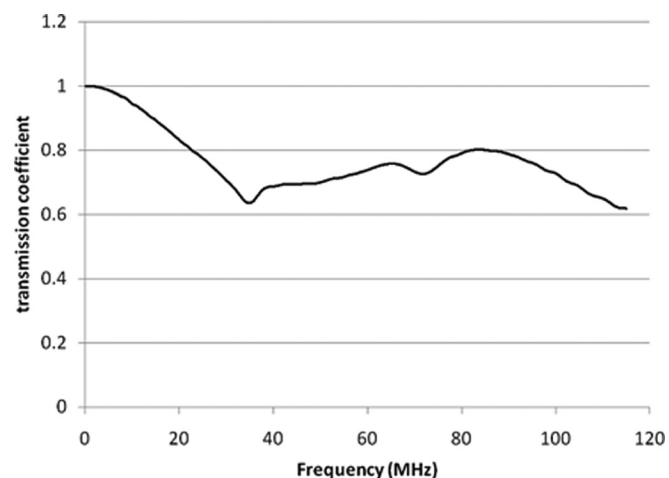


FIG. 8. Round-trip water-Saran-water transmission coefficient vs. frequency. Individual curves from transducers of different center frequencies have been combined.

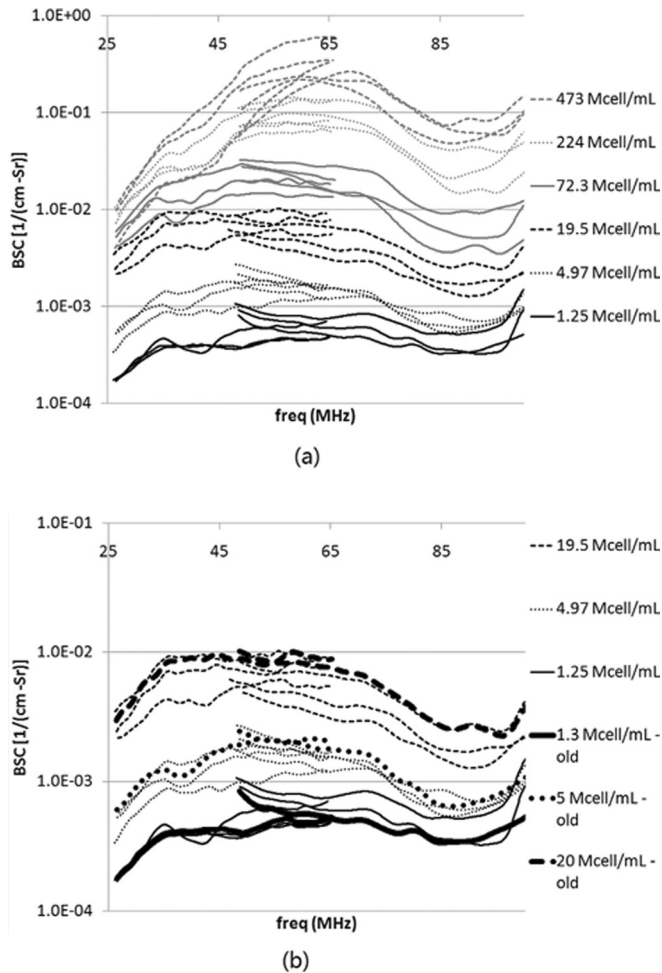


FIG. 9. (a) Estimated BSC vs. frequency for all cell pellets. Estimated BSC of each cell pellet sample is based on data acquired from two transducers: 40 MHz and 80 MHz. The legends represent number density. There are three cell pellets per number density. (b) Comparison between the new and the old BSC data for three low concentrations. The new data are the data obtained in this study. The old data are the data in the previous publication (Fig. 6, Teisseire *et al.*, 2010).

pathway and was held such that the Saran was parallel to the Plexiglas surface. The distance between the Saran and Plexiglas surface was 1.6 mm so that the diffraction caused by the insertion of Saran was negligible. The following equation is used to calculate the transmission coefficient through water-Saran-water interface (round-trip, the pulse transmitted through the Saran layer twice in this experimental setup):

$$T(f) = \frac{S_s(f)}{S_r(f)}, \quad (7)$$

where $T(f)$ is the frequency-dependent transmission coefficient, $S_r(f)$ is the amplitude spectrum of the reference signal and $S_s(f)$ is the amplitude spectrum of the reflected signal from the Plexiglas when the Saran is placed above the Plexiglas. The measured curve is not a cosinusoid-like curve as predicted by the three-layer transmission theory [Wear *et al.*, 2005, Eq. (3)]. The measured curve was directly used for transmission compensation, without being fitted to any theoretical model.

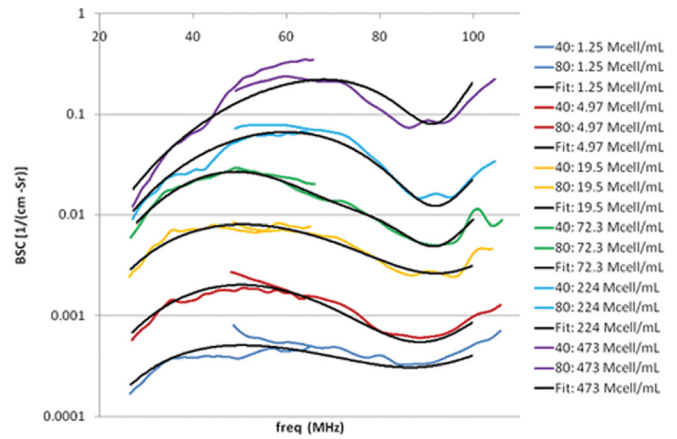


FIG. 10. (Color online) Fitted BSC of CHO cell pellets compared with the BSC estimates. The smooth black lines represent the fitted BSC relative to the concentric sphere model. Only one representative cell pellet sample per number density is shown for figure simplicity.

D. BSC results

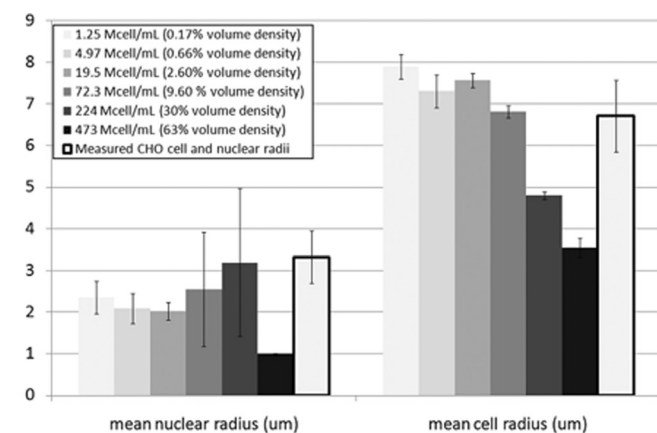
BSC estimates of all the cell pellets in this study are shown in Fig. 9(a). The BSC vs. frequency curves for different concentrations share a similar pattern in the sense that a peak in the BSC magnitude is followed by a dip, as frequency increases. In spite of that, the BSC changes with increasing number density: the BSC magnitude increases; the dynamic range of BSC increases; and the positions of the peak and dip vary slightly. Thus, number density affects both the magnitude and the shape of BSC.

Because the three lower concentrations are the same as the previous study, a comparison between the current and the former BSC data is provided [Fig. 9(b)]. The BSC estimates in the two studies are consistent. The repeatability of the results indicates that this biophantom methodology could be a useful technique of evaluating scattering models for biological materials.

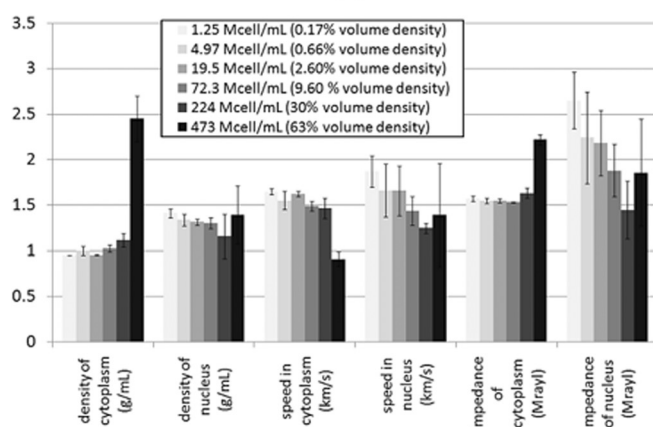
E. Least squares parameter estimates

The best-fit theoretical BSCs of all biophantom samples are calculated using the least squares technique; each biophantom was scanned with two transducers (Table I). Figure 10 provides an indication of how the fitted BSC curves (one fitted BSC curve for each biophantom) are compared to the BSC estimates. It could be observed from this figure that the highest concentration has the worst fit. The estimated parameters of the theoretical models are summarized in Fig. 11. The mean values are averages of the three cell pellets for each cell concentration. The standard deviations are calculated based on the three samples per concentration.

The estimated cell radii agree well with the directly measured radii for low-concentration conditions (1.25, 4.97, 19.5, 72.3 Mcell/mL), showing that the combination of concentric spheres model and least squares method makes it possible to predict cell radius using the BSC information. For higher concentration cell pellets (224, 473 Mcell/mL), the cell radius has been underestimated. In fact, Fig. 11(a) shows that the estimated cell radius decreases as the cell



(a)



(b)

FIG. 11. Summary of the estimated fit parameters given by the theoretical concentric sphere BSC calculations: (a) estimated vs. measured nuclear and cell radii, (b) estimated acoustic properties of the cell nucleus and cytoplasm.

concentration increases except for the 19.5 Mcell/mL case (7.9, 7.3, 7.6, 6.8, 4.8, 3.6 μm for 1.25, 4.97, 19.7, 72.3, 224, 473 Mcells/mL cell pellets, respectively). The underestimate of the cell radius when the cell concentration is large suggests that at high cell concentration either the cells can no longer be modeled as concentric spheres (structural and shape changes) or the total intensity cannot be calculated as the sum of the individual cells intensities (coherent scattering and multiple scattering) or perhaps both. Either way indicates that the concentric spheres model is losing its applicability for large cell concentrations.

In terms of the estimated speed of sound, density, and acoustic impedance, discrepancy exists between the values estimated for the lower concentrations in this study and those in the previous work (Teisseire *et al.*, 2010). For instance, the estimated acoustic impedance of the nucleus for the lower concentrations in this paper ranges between 1.9 and 2.6 Mrayl, whereas the value is close to 1.6 Mrayl in the previous publication. There could be several reasons for this discrepancy. First, the methods of processing the data are different. The uniform size distribution was used previously. The estimated parameters are from one realization per number density. In the present study, the Gaussian size

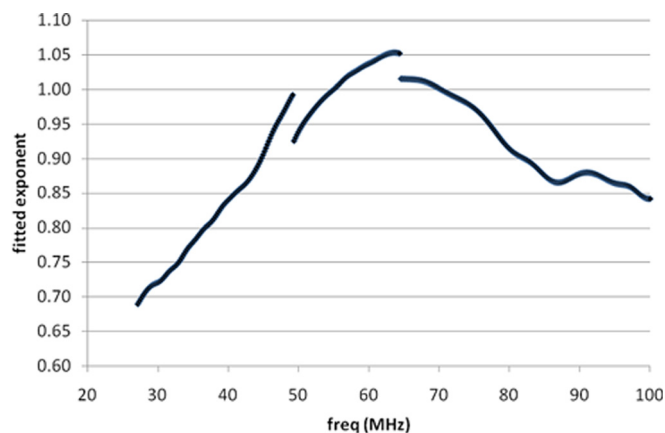


FIG. 12. (Color online) Fitted power exponent as a function of frequency.

distribution is used, and the estimated parameters are averages of three realizations per number density. Second, the discrepancy could be a sign that the BSC is more sensitive to the cell sizes but less sensitive to the speeds and densities. Therefore, the concentric sphere model is not ideal in determining the speeds and densities from BSC.

The fitted parameters for the largest concentration seem to be outliers. Those values are actually beyond the range of reasonable values. For instance, the estimated density of cytoplasm is greater than 2 g/mL, and the estimated sound speed in cytoplasm is less than 1000 m/s. Such values are not in agreement with density and sound speed in water. Because the cytoplasm contains mainly water, reasonable properties of cytoplasm should be close to those of sea water, as is also shown by the estimates from cell pellets of other concentrations. The deviation of estimated parameters from reasonable values at high cell concentration is a further indication that at high cell concentration either the cells can no longer be modeled as concentric spheres or the total intensity cannot be calculated as the sum of the individual cells intensities, or both.

F. BSC magnitude vs. number density

Besides frequency dependence, the BSC magnitude also appears to provide important information. The BSC magnitude increases with cell concentration, as is qualitatively shown in Fig. 9(a). In fact, Eq. (2) predicts that BSC is linearly proportional to number density. To investigate whether that prediction is observed, the BSC as a function of number density is fitted to the power law relationship. The fitted power exponent as a function of frequency is displayed in Fig. 12. The curve has three discontinuous segments because data from different transducers are used. The data from the 40 and 80 MHz transducers are used for the left and right segments, respectively, whereas the middle segment is determined using the data from both transducers (the data from both transducers were averaged). The fitted power exponent is an indicator of how the BSC changes with number density. If the BSC is linearly proportional to number density, then the fitted power exponent will be unity. Figure 12 indicates that BSC is not linearly proportional to number density. The BSC increases less than linear with number density below

50 MHz and above 70 MHz, whereas it increases greater than linear with number density around 60 MHz.

The observed BSC vs. concentration relationship (fitted power exponent being less than unity) at low frequency has been found previously in blood characterization and physical phantom studies. For instance, [Shung et al. \(1984\)](#) found that the backscattered power drops when the concentration of erythrocytes in blood surpasses 30%. Similar finding was also reported by [Chen et al. \(1996\)](#) for physical phantoms. Those previous findings are in the Rayleigh region and have been attributed to coherent scattering because when the scatterer volume fraction is high, the assumption of a random distribution of scatterers fails due to the correlation among the scatterers. Thus the BSC vs. concentration relationship at low frequency (Rayleigh region) found in our experiment might also be attributed to coherent scattering. What is new in our result is that at 60 MHz where the wavelength is comparable to cell size ($ka \approx \pi/2$, where k is acoustic wave number and a is cell radius), the BSC increases approximately linearly (fitted power exponent is 1.04) as the concentration becomes high. At 90 MHz, the BSC starts to increase slower again for high concentrations. Therefore, instead of simply decreasing BSC as is in the case of Rayleigh scattering, the cell concentration has a more complicated effect on BSC when wavelength is comparable to the scatterer size.

V. DISCUSSION

The shape of measured BSC vs. frequency curves, the least squares concentric sphere model estimates and the observed BSC magnitude vs. number density relationships all suggest that the concentric sphere model is good for low concentrations but starts to break down at high cell concentration because the acoustic scattering becomes more complicated. There are a number of possible explanations for this observation. First, coherent scattering may play a role because the assumption of random position of cells may no longer be true as the cells get close to each other. The possible regularity of cell positions can have either constructive or destructive effect on the total scattered energy depending on the frequency. Using this hypothesis, we may conclude that the effect of coherent scattering is mainly destructive in the 20 to 100 MHz frequency range except for the frequencies around 60 MHz (Fig. 12). Second, the scattering site may start to change. For example, the background medium becomes isolated by cells, which makes it possible that the background medium effectively becomes the scattering source. It is also possible that the main interface responsible for the scattering is between the nucleus and cytoplasm of the cells, whereas in the lower concentrations it is primarily the cytoplasm-background boundary. This possibility is supported by the decreasing trend of fitted radii with increasing number density. Third, multiple scattering may also play a role considering how close the cells are to each other. Additionally, the shape of cells may start to change as well when they are getting closer to one another.

The above results and discussion have suggested that the concentric sphere model is not applicable at high

concentrations. Then when does the model start to be adversely affected by the high concentration effect? From our results, the parameter estimates of the 72.3 Mcell/mL (volume density 10%) CHO cell pellet does not seem to be affected, while the parameter (cell radius) estimate of the 224 Mcell/mL (volume density 30%) cell pellets is affected (e.g., cell radius is underestimated). Therefore, it is suggested that the critical volume density is between 10% and 30%.

VI. CONCLUSIONS

The acoustic scattering at high cell concentration is more complicated than that at low concentration. The low cell concentration parameter estimates appear to yield reasonable size and composition values. The high cell concentration has a significant impact on the measured backscatter coefficients for which the concentric sphere model starts to break down. The critical volume density, starting from when the model becomes inapplicable, is between 10% and 30%. Above this critical volume density, another scattering model is likely to be effective.

ACKNOWLEDGMENTS

This work was supported by NIH Grant R01CA111289. The authors would like to thank Saurabh Kukreti, Michael Kurowski, Matt Lee, and Eugene Park from the University of Illinois at Urbana-Champaign for their assistance with data acquisitions and attenuation measurements.

- Aubry, A., Derode, A., and Tanter, M. (2008). "Extraction of the multiple scattering contribution in weakly scattering media: Application to human soft tissue," *J. Acoust. Soc. Am.* **123**, 3001.
- Aubry, A., and Derode, A. (2011). "Multiple scattering of ultrasound in weakly inhomogeneous media: Application to human soft tissues," *J. Acoust. Soc. Am.* **129**, 225–233.
- Anderson, V. C. (1950). "Sound scattering from a fluid sphere," *J. Acoust. Soc. Am.* **22**, 426–431.
- Anderson, J. J., Herd, M.-T., King, M. R., Haak, A., Hafez, Z. T., Song, J., Oelze, M. L., Madsen, E. L., Zagzebski, J. A., O'Brien, W. D., Jr., and Hall, T. J. (2010). "Interlaboratory comparison of backscatter coefficient estimates for tissue-mimicking phantoms," *Ultrasonic Imaging*, **32**, 48–64.
- Baddour, R. E., Sherar, M. D., Hunt, J. W., Czarnota, G. J., and Kolios, M. C. (2005). "High-frequency ultrasound scattering from microspheres and single cells," *J. Acoust. Soc. Am.* **117**, 934–943.
- Chen, J., and Zagzebski, J. A. (1996). "Frequency dependence of backscatter coefficient versus scatterer volume fraction," *IEEE Trans. Ultrason. Ferroelectr. Freq. Control*, **43**, 345–353.
- Chen, X., Phillips, D., Schwarz, K. Q., Mottley, J. G., and Parker, K. J. (1997). "The measurement of backscatter coefficient from a broadband pulse-echo system: A new formulation," *IEEE Trans. Ultrason. Ferroelectr. Freq. Control*, **44**, 515–525.
- Czarnota, G. J., and Kolios, M. C. (2010). "Ultrasound detection of cell death," *Imaging Med.* **2**, 7–28.
- Daport, A., King, M. R., Harter, J., Sarwate, S., Oelze, M. L., Zagzebski, J. A., Do, M. N., Hall, T. J., and O'Brien, W. D., Jr. (2011). "Analysis of human fibroadenomas using Three-Dimensional Impedance Maps," *IEEE Trans. Med. Imaging* **30**, 1206–1213.
- Doyle, T. E., Tew, A. T., Warnick, K. H., and Carruth, B. L. (2009). "Simulation of elastic wave scattering in cells and tissues at the microscopic level," *J. Acoust. Soc. Am.* **125**, 1751–1767.
- Duck, F. A. (1990). *Physical Properties of Tissue: A Comprehensive Reference Book* (Academic Press, London), Chap. 4, p. 95.
- Falou, O., Rui, M., Kaffas, E. I., Kumaradas, J. C., and Kolios, M. C. (2010). "The measurement of ultrasound scattering from individual micron sized objects and its application in single cell scattering," *J. Acoust. Soc. Am.* **128**, 894–902.

- Hunt, J. W., Worthington, A. E., Xuan, A., Kolios, M. C., Czarnota, G. J., and Sherar, M. D. (2002). "A model based upon pseudo regular spacing of cells combined with the randomisation of the nuclei can explain the significant changes in high-frequency ultrasound signals during apoptosis," *Ultrasound Med. Biol.* **28**, 217–226.
- King, M. R., Anderson, J. J., Herd, M.-T., Ma, D., Haak, A., Madsen, E. L., Zagzebski, J. A., Oelze, M. L., Hall, T. J., and O'Brien, W. D., Jr. (2010). "Ultrasonic backscatter coefficients for weakly scattering, agar spheres in agar phantoms," *J. Acoust. Soc. Am.* **128**, 903–908.
- Kolios, M. C., Czarnota, G. J., Worthington, A. E., Giles, A., Tunis, A. S., and Sherar, M. D. (2004). "Towards understanding the nature of high frequency backscatter from cells and tissues: An investigation of backscatter power spectra from different concentrations of cells of different sizes," in *Proceedings of the 2004 IEEE Ultrasonics Symposium*, pp. 606–609.
- Mamou, J., Oelze, M. L., O'Brien, W. D., Jr., and Zachary, J. F. (2005). "Identifying ultrasonic scattering sites from three-dimensional impedance maps," *J. Acoust. Soc. Am.* **117**, 413–423.
- McNew, J., Lavarello, R., and O'Brien, W. D., Jr. (2009). "Sound scattering from two concentric fluid spheres," *J. Acoust. Soc. Am.* **122**, 2968–2968.
- Oelze, M. L., and Zachary, J. F. (2006). "Examination of cancer in mouse models using high-frequency quantitative ultrasound," *Ultrasound Med. Biol.* **32**, 1639–1648.
- Pawlicki, A. D., Dapore, A. J., Sarwate, S., and O'Brien, W. D., Jr. (2011). "Three-dimensional impedance map analysis of rabbit liver," *J. Acoust. Soc. Am.* **130**, EL334–EL338.
- Shung, K. K., Yuan, Y. W., Fei, D. Y., and Tarbell, J. M. (1984). "Effect of flow disturbance on ultrasonic backscatter from blood," *J. Acoust. Soc. Am.* **75**, 1265–1272.
- Saha, R. K., and Kolios, M. C. (2010). "Simulation of ultrasound backscattering by red cell aggregates: Effect of shear rate and anisotropy," in *Proceedings of the 2010 IEEE Ultrasonics Symposium*, pp. 2307–2310.
- Taggart, L. R., Baddour, R. E., Giles, A., Czarnota, G. J., and Kolios, M. C. (2007). "Ultrasonic characterization of whole cells and isolated nuclei," *Ultrasound Med. Biol.* **33**, 389–401.
- Teisseire, M., Han, A., Abuhabsah, R., Blue, J. P., Jr., Sarwate, S., and O'Brien, W. D., Jr. (2010). "Ultrasonic backscatter coefficient quantitative estimates from Chinese hamster ovary cell pellet biophantoms," *J. Acoust. Soc. Am.* **128**, 3175–3180.
- Tunis, A. S., Baddour, R. E., Czarnota, G. J., Giles, A., Worthington, A. E., Sherar, M. D., Kolios, M. C. (2005). "Using high frequency ultrasound envelope statistics to determine scatterer number density in dilute cell solutions," in *Proceedings of the 2005 IEEE Ultrasonics Symposium*, pp. 878–881.
- Vlad, R. M., Saha, R. K., Alajez, N. M., Ranieri, S., Czarnota, G. J., Kolios, M. C. (2010). "An increase in cellular size variance contributes to the increase in ultrasound backscatter during cell death," *Ultrasound Med. Biol.* **36**, 1546–1558.
- Wear, K. A., Stiles, T. A., Frank, G. R., Madsen, E. L., Cheng, F., Feleppa, E. J., Hall, C. S., Kim, B. S., Lee, P., O'Brien, W. D., Jr., Oelze, M. L., Raju, B. I., Shung, K. K., Wilson, T. A., and Yuan, J. R. (2005). "Interlaboratory comparison of ultrasonic backscatter coefficient measurements from 2 to 9 MHz," *J. Ultrasound Med.* **24**, 1235–1250.